ARTICLE

Designed TiS_2 nanosheets efficient for electrocatalytic reductive amination of biomass-derived furfurals

TON6 Received 00th January 20xx,
Accepted 00th January 20xx

DOI: 10.1039/x0xx00000x

Man Zhang,‡[a] Shaojun Xu,‡[b,c] Mebrouka Boubeche,[d] Donato Decarolis,[b,c] Yizhe Huang,[a] Biying Liu,[a] Emma K. Gibson,[c,e] Xin Li,[a] Yuchen Wang,[a] Huixia Luo,[d] C. Richard A. Catlow*[b,c,f] and Kai Yan*[a]

Abstract: Green and highly selective synthesis of organonitrogen chemicals (ONC) using renewable energy source of biomass over noble-metal free solid catalyst under common room temperature and pressure conditions is still a major challenge. Here, we report a sustainable electrochemical method for the selective synthesis of several valuable ONC with high yield using biomass-derived furanic aldehydes over greenly fabricated TiS_2 nanosheets through the facile synthesis. Based on a range of characterization techniques including high-resolution transmission electron microscopy and X-ray absorption fine structure, a well-defined structure of TiS_2 nanosheets (3.86 nm with 1T phase) is constructed. These as-prepared catalysts are applied to the electrochemical reductive amination (ERA) of three biomass-derived aldehydes, i.e. furfural (FF), 5-methylfurfural (MF) and 5-hydroxymethylfurfural (HMF), and exhibit superior performance whereby over 95% conversion of each furanic aldehyde and nearly perfect selectivity of ONC are achieved. TiS_2 nanosheets, in particular, possess a marked ~2-fold increase in conversion (~49%) compared with its monometallic Ti electrode. Besides, reaction kinetics and rational pathway are also studied. In addition, these exfoliated TiS_2 nanosheets maintain high durability over 6 h, providing a promising and versatile route for the sustainable upgrading of biomass-derived sources.

Introduction

Organonitrogen chemicals (ONC) are crucial platform chemicals for manufacturing dyes, pharmaceuticals, drug intermediates, surfactants and agrochemicals.[1-4] It was reported that over 80% of the top 200 pharmaceuticals were derived from amines in 2020.[5, 6] The conventional synthesis of ONC is mainly from alkyl halides, nitro complexes, or nitriles, with which many by-products and waste are associated.[7-9] The direct reductive amination of aldehydes with ammonia or organic amines has been envisioned as an alternative for ONC production.[10, 11] In particular, aldehydes could be readily produced from renewable biomass resources and water is the sole by-product of the reaction, reducing the carbon footprint.[12, 13]

The selective synthesis of ONC remained a big challenge due to the easily occurred side reactions.[14-20] Taking the furanic aldehydes for example, the amination reaction involved a complicated pathway as depicted in Scheme 1. The target ONC could be selectively generated from the condensation of furanic aldehydes (a) with ethanolamine through C-N coupling and then via the hydrogenation of primary imine to ONC.[11] As illustrated in scheme 1, when the main reaction of target ONC (c) took place, the direct hydrogenation and/or hydrogenolysis of furanic aldehydes to alcohols (d) and furans (e) would compete with the reaction pathway of ONC. The progress of robust catalysts and catalytic system for the process are of great importance for the syntheiss of ONC.[21-24]

So far, the most widely used catalysts contain noble metals (e.g. Ru, Pt, Pd, Rh, and Au) through traditional synthesis.[25-30]. Gross *et al.* reported the efficiency of reductive amination of

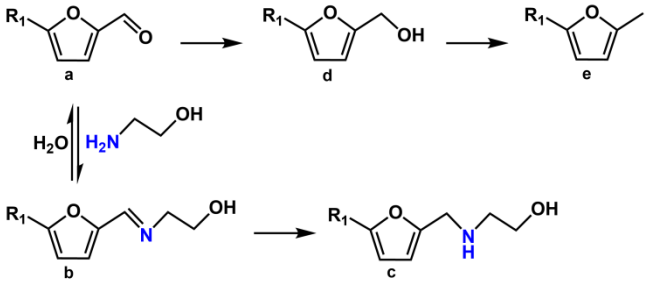

Scheme 1. Reaction process for the reductive amination of furanic aldehydes. The target product organonitrogen chemicals (ONC, c) from furanic aldehydes (a) amination is obtained, wherein a series of side reactions (a-e) may involve. (R_1 is hydrogen, methyl-, ethyl-, and hydroxymethyl).

[a] School of Environmental Science and Engineering, Guangdong Provincial Key Laboratory of Environmental Pollution Control and Remediation Technology, Sun Yat-sen University, Guangzhou 510275, China
[b] School of Chemistry, Cardiff University, Main Building, Park Place, Cardiff, CF10 3AT, United Kingdom
[c] UK Catalysis Hub, Research Complex at Harwell, Rutherford Appleton Laboratory, Harwell, OX11 0FA, United Kingdom
[d] School of Materials Science and Engineering and Key Lab Polymer Composite & Functional Materials, Sun Yat-sen University, Guangzhou, 510275, China
[e] School of Chemistry, Joseph Black Building, University of Glasgow, Glasgow G12 8QQ, United Kingdom
[f] Department of Chemistry, University College London, 20 Gordon Street, London, WC1H 0AJ, United Kingdom
*Corresponding author E-mail address: c.r.a.catlow@ucl.ac.uk (C. Richard A. Catlow); yank9@mail.sysu.edu.cn (K. Yan)
† Electronic Supplementary Information (ESI) available: See DOI: 10.1039/x0xx00000x
‡ These authors contributed equally to this work.

benzaldehyde to benzylamine on the homogeneous Rh catalyst at 135 °C and 6.5 MPa reducing gas.[31] Mei *et al.* considered the electrosynthesis method at 70 °C.[32] They discovered that C-H bond amination in organopalladium intermediates produced an ONC product with 82% yield. However, these described catalysts exhibited a fair amount of the amine selectivity. Some metal electrodes of Pt, Cu, Ag etc. exhibited high selectivity (nearing 100%) through electrochemical reduction avoiding the high temperature.[33] The enhancing selectivity largely depended on the metal special active capacity.[34, 35] It was highly desirable, therefore, to develop improved protocols for synthesizing ONC using an inexpensive catalyst.

Low-cost transition metal dichalcogenides,[36] which were a new family of 2D nanosheets, were promising candidates due to their wide operational voltage, long cycle-life, high surface ions diffusivities, and ultrafast charge/discharge capabilities.[37-43] Recent efforts have been made to utilize transition metal dichalcogenides (e.g, MoS_2, TaS_2) for hydrogen evolution reaction.[34, 44-47] However, few studies have utilized transition metal dichalcogenides catalysts for the sustainable synthesis of ONC from biomass-derived furanic aldehydes.

Here, we documented a sustainable method for electrochemical reductive amination (ERA) of various furanic aldehydes over TiS_2 nanosheets at room temperature and pressure (as illustrated in Fig. 1). TiS_2 nanosheets were firstly fabricated through the solid-state synthesis without the use of organic solvents, and then exfoliated by 10 mL isopropanol. The physical properties of the obtained TiS_2 were then characterized using high-resolution transmission electron microscopy (HR-TEM), electron paramagnetic resonance (EPR), and X-ray absorption fine structure (XAFS) analysis. These as-prepared TiS_2 nanosheets exhibited superior performance for ERA of three biomass-derived furfural (FF), 5-methylfurfural (MF) and 5-hydroxymethylfurfural (HMF) in 0.7 M ethanolamine. Over 95% conversion of furanic aldehydes, nearing perfect selectivity of ONC, and good turnover number (TON) and high stability were achieved. The results showed a marked ~2-fold improvement of furfural conversion on comparison with Ti electrode (< 50 %). These controllably synthesized laminate TiS_2 nanosheets offer the following benefits: (i) thin nanosheets, supplying sufficient surface active centres, (ii) a large electrochemical active surface area (ECSA), small Tafel slope and faster kinetics, (iii) a high concentration of sulfur vacancies, enhancing the adsorption of reactants, (iv) high stability and good durability over 6 h.

Results and discussion

Characterization of laminate TiS_2 nanosheets

The morphology and surface textural properties of the as-synthesized laminate TiS_2 nanosheets were firstly determined using transmission electron microscopy (TEM), as detailed in the electronic supplementary Information (ESI). TEM images (Fig. S1a and b †) showed a typical layered structure of transition metal dichalcogenides. The high-resolution HR-TEM image (Fig. 2a) of TiS_2 showed the characteristic lattice fringes of the (001) plane with the lattice spacing of 0.569 nm. In addition, the ring and spot in the selected area electron diffraction (SAED) confirmed the structure of TiS_2. As shown in Fig. 2b, the well-defined rings could be indexed into the (001), (101), (102), (110), (103), (004) and (202) planes of TiS_2. Moreover, the interplanar spacing of 0.569 and 0.262 nm were measured in an enlarged view of Fig. 2c corresponding to the (001) and (101) plane of TiS_2. In addition, the HR-TEM image in Fig. S2a† showed that TiS_2 is located on the ⟨100⟩ zone axis, as

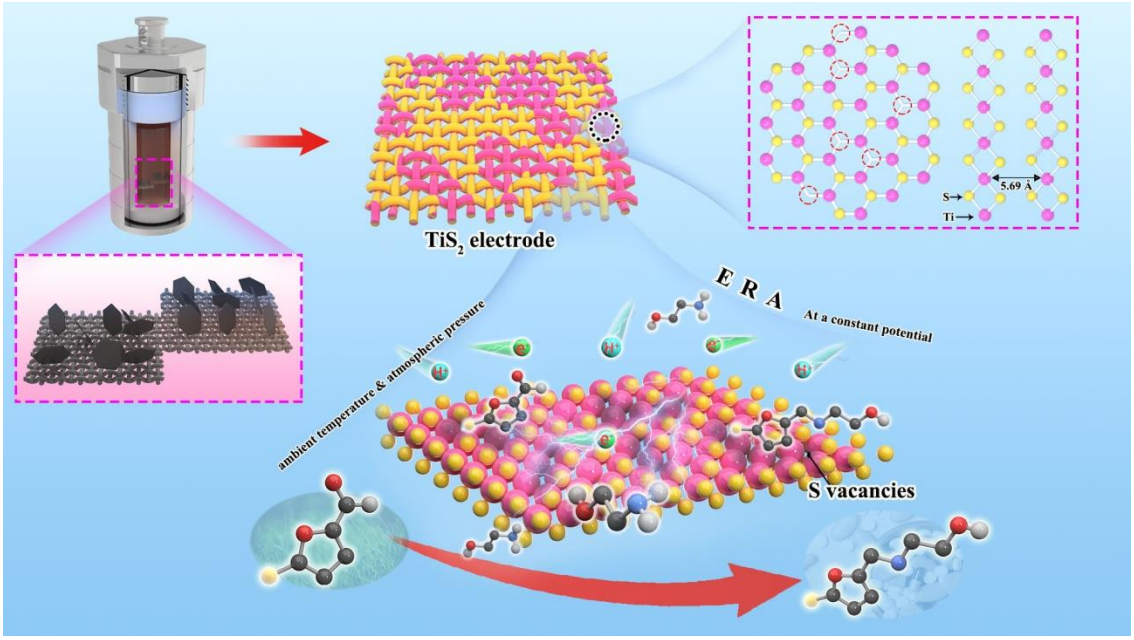

Fig. 1 Schematic view of the controllable synthesis of TiS_2 nanosheets electrode and the ERA reaction.

the schematic view of the TiS_2 crystal lattice (Fig. S2b†). The energy-dispersive X-ray spectroscopy (EDS) analysis showed the uniform distribution of Ti and S as displayed in Fig. 2d-2f. Moreover, the atomic force microscopy (AFM) analysis (Fig. 2g) shows that laminate TiS_2 nanosheets had an average thickness of 3.86 ± 0.17 nm (Fig. 2h). As shown in Fig. S3†, the height profile had a mean value of 3.86 nm, indicating that laminate TiS_2 nanosheets comprised 6-8 layers.

The as-synthesized TiS_2 was further characterized by powder X-ray diffraction (XRD), as detailed in the ESI†. In Fig. S4a†, the characteristic signals in the diffractogram of TiS_2 were well-indexed to a hexagonal structure (JCPDS card no. 15-0853). The Bragg positions correspond with the P3 m1 (No. 164) space group (a = 3.405 Å, b = 3.405 Å, and c = 5.691 Å).[48] In addition, Raman spectroscopy was utilized to investigate the surface bond of TiS_2 as an effective tool to study defects. In general, TiS_2 had two Raman active modes: in-plane vibrational mode (E_g) and out-of-plane mode (A_{1g}).[49, 50] However, the as-synthesized TiS_2 showed two main peaks at 228 cm^{-1} and 330 cm^{-1} (assigned to E_g and A_{1g}), but also a "shoulder peak" at 382 cm^{-1} (Fig. S4b†). The "shoulder peak" suggested the stiffened phonon modes responsible for the temperature-dependent scattering because of the appearance of sulfur vacancies in the TiS_2 material.[51, 52] The schematic structure of TiS_2 was depicted in Fig. S4b†, the Ti atom layer was located in the middle of the two S atom layers with which it formed covalent bonds. After that, the van der Waals interactions held the S-Ti-S layers together. TiS_2 material was the 1T phase based on the stacking ordering of S-Ti-S layers along the c axis (vertical direction).[53] This unique two-dimensional spacing structure was beneficial to allow ready diffusion and transport of platform molecules (e. g., FF, MF and HMF).

To obtain an understanding of surface defects, EPR was executed to study the spin states of TiS_2 as detailed in the SI. The results are shown in Fig. 3a. Laminate TiS_2 nanosheets revealed a strong EPR peak at g = 2.003, which corresponds to more exposed active centres due to sulfur vacancies.[54, 55] Furthermore, the chemical status of the Ti-S bond and the local structure of the metal cations were investigated by analysis of the X-ray absorption fine structure (XAFS) collected at the Ti K-edge (Fig. 3b). X-ray absorption near-edge structure (XANES) spectra of as-prepared TiS_2 compares well with the standard TiS_2 reference. A reasonable fit of the Fourier transform of the k^2 weighted XAFS data (Fig. 3c and 3d) was obtained using Ti-S scattering paths at 2.43 ± 0.02 Å for as-synthesized TiS_2. This distance was consistent with that obtained for standard TiS_2 reference at 2.40 ± 0.02 Å (Table S1†). It was noted that the intensity of the feature at low R in the Fourier Transform, for the as-synthesized TiS_2 was lower than that of a TiS_2 reference material, in agreement with the

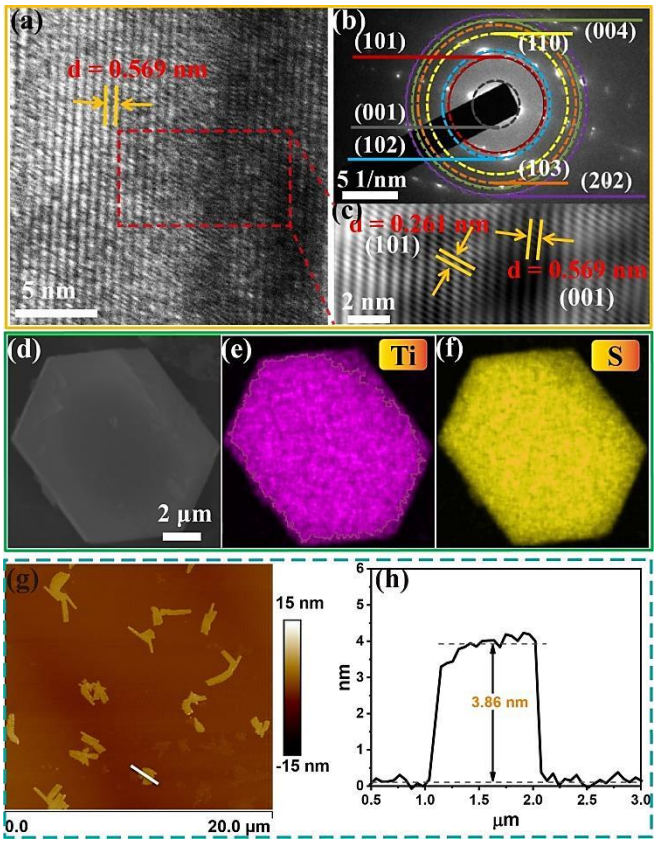

Fig. 2 (a) HR-TEM image, (b) SAED pattern, (c) corresponding inverse fast Fourier transform (FFT) image of areas in red frame in (a), and (d, e, f) elemental mapping of the as-synthesized TiS_2. AFM image (g) and height profile (h) of TiS_2.

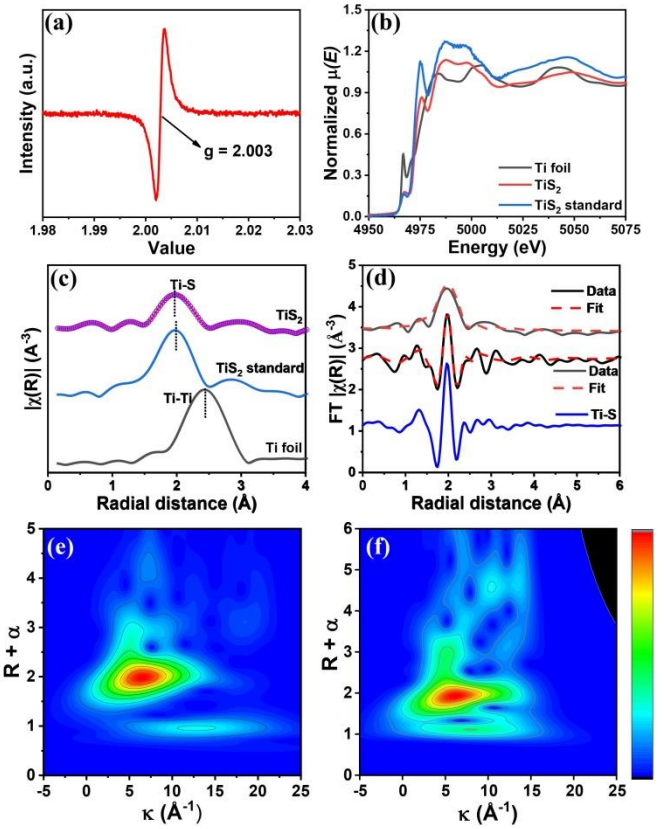

Fig. 3 (a) EPR spectrum of TiS_2, (b) normalized Ti K-edge XANES spectra of as-synthesized TiS_2 and standard XANES spectra of Ti foil and TiS_2 recorded as references, (c) non-phase corrected Fourier-transformed k^2 weighted XAFS of as-synthesized TiS_2 and the standard TiS_2 as references, (d) Stacked plots of the magnitude (top) and imaginary (bottom) non-phase corrected Fourier-transformed Ti K-edge XAFS. XAFS wavelet transforms spectra of (e) commercial TiS_2 and (f) the as-synthesized TiS_2.

XAFS fit of the 1st shell Ti-S path giving coordination numbers of (3.1 ± 0.8) and (4 ± 1) for as-synthesized TiS_2 and standard TiS_2 reference, respectively (Table S1†). That implied the presence of sulfur vacancies, exposing more metal active sites. In addition, the wavelet transforms (WT) analysis of Ti XAFS oscillations was conducted. For the WT contour plot of TiS_2 (Fig. 3e and f), one intensity maximum at near ~4 $Å^{-1}$ was observed, which was assigned to the Ti-S contribution.

Electrochemical reductive amination (ERA)

To evaluate these fabricated catalysts, ERA reactions of furanic aldehydes over TiS_2 electrode were firstly examined by scanning linear sweep voltammetry (LSV) curves in a three-electrode system. The change of cathodic current was obtained in ethanolamine electrolyte with and without 5 mM furfural (FF) as shown in Fig. 4a. In the absence of FF, the cathode current was attributed to the reduction of water to generate H_2.[33] After adding 5 mM FF into ethanolamine, the onset current increases, and a positive 160 mV shift in the onset potential was observed. Also, before water reduction, there was a well-defined diffusion-limited reduction peak for aldimine, which suggested that the ERA of FF was more favoured over water reduction on the TiS_2 nanosheets. Although there was no obvious onset shift in the LSV curves for TiS_2 electrode with and without 5-methylfurfural (MF), the current density gradually increases at the implemented potential range of E < -0.4 V vs. RHE (V_{RHE}) by equation S1†. These results indicated that the aldimine reduction had slow dynamics equivalent to water reduction in ethanolamine containing 5 mM MF on the TiS_2 nanosheets electrode. Meanwhile, blank carbon fibre paper and Ti foil as working electrodes for ERA were compared and considered. LSV curves were shown in Fig. S5†, exhibiting poor current efficiency. The result indicated that TiS_2 showed high-efficient metal sites for ERA due to the sulfur vacancies. Additionally, the Tafel slope was given in Fig. 4b, exhibiting fast dynamic interaction of ERA with and without furanic aldehydes. The Tafel slope (300 mV dec^{-1}) after adding FF was lesser than that of pure water reduction without FF (375 mV dec^{-1}), suggesting the accelerated dynamics of ERA reaction. In Fig. S6, the furfurals adsorption peaks were obvious in LSV curves at a slow scan rate of 2 mV s^{-1}.

The electrochemical active surface area (ECSA) for the three furanic aldehydes was also studied to understand the effect of the catalysts surface adsorption capacity on electrochemical reductive amination reactions (Fig. S7a-7c†). Electrochemical double-layer capacitance (Fig. S7d†) values via equation S2† were 0.13, 0.11, and 0.12 mF cm^{-2} in FF, MF, and HMF, respectively. Furthermore, laminate TiS_2 nanosheets yielded ECSA (equation S3†) of 3.25 cm^2 within FF, 2.75 cm^2 in MF and 3.00 cm^2 in HMF. After ERA, ECSA values were 3.25, 2.72, and 2.95 cm^2, respectively. These further confirmed that laminate TiS_2 nanosheets exhibited high activity area in ERA.

In addition, the mass activity was estimated using equation S4† as shown in Fig. 4c. Notably, there was a result that the mass activity in FF_5 was superior to those in MF and HMF at the applied potential of -0.3~-0.6 V_{RHE}. Especially, at the applied potential of -0.3 V_{RHE}, the mass activity of 1.23 mA mg^{-1} in FF was 3.0 and 2.1 times greater than those in MF (0.41 mA mg^{-1}) and HMF (0.59 mA mg^{-1}). However, at -0.7 and -0.8 V_{RHE}, the mass activity was approximately equal for the different

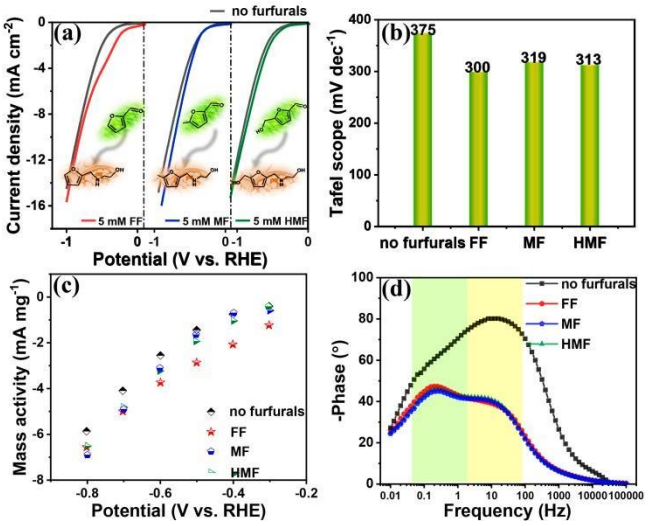

Fig. 4 (a) LSV curves of TiS_2 electrode in 0.7 M ethanolamine electrolyte (no furfurals) and ethanolamine containing 5 mM FF at scan rate 5 mV s^{-1}; Likewise, LSV curves in 5mM MF and in 5mM HMF. (b) Corresponding Tafel scope. (c) Mass activity of TiS_2 electrode in diverse electrolytes at different applied potentials. (d) Bode plots in ethanolamine electrolyte and with FF, MF, HMF, respectively.

furanic aldehydes, implying the low current efficiency at a high applied potential. Besides, the bold plots in Fig. 4d show the ridge peaks in the ethanolamine containing 5 mM FF (or MF, or HMF) at a low frequency interface, compared with only one peak curve in the curve in pure ethanolamine. These results indicated that ERA reactions had a higher priority and were efficient with addition of FF (or MF, or HMF). The low overpotential, small Tafel slope and large ECSA suggested that the TiS_2 nanosheets electrode exhibits a high ERA activity.

The turnover frequency (TOF, Fig. S8a†) for the three reductive aminations over TiS_2 nanosheets at -500 mV was computed using equation S5† to highlight the intrinsic reduction activity in detail. In particular, the computed TOF value of 0.407 s^{-1} for 5 mM FF was significantly greater (pure water oxidation of 0.205 s^{-1}). These results suggested that the TOF of FF was nearly 2 times greater than that of no furfurals, further indicating that the ERA is the dominant reaction.

The effect of applied potential on the reduction of three furanic aldehydes over TiS_2 nanosheets is shown in Fig. S8b† and Table 1. The average current density of 1.45 mA cm^{-2} in FF was much higher than the value of 0.82 mA cm^{-2} in MF and 1.24 mA cm^{-2} in HMF at the potential of -0.4 V_{RHE}. The concentration of furan aldehydes decreased gradually over 6 h for each of the products produced from the reductive amination, with the respective products having HPLC retention time of 5.4 min (FF), 8.2 min (MF) and 4.8 min (HMF) in Fig. S9†. To identify reaction intermediates, the standard curves of FF, MF and HMF (Fig. S10†) and ultra-performance liquid chromatography /tandem mass spectrometry (UPLC-MS/MS) was carried out, as described in the Experimental section. In the MS spectrum (Fig. S11a†), the mass-to-charge ratio (m/z) of 141.16 was confirmed as the amine product 5-(ethanolaminemethyl) furan (EMF) from FF. The m/z of 121.02 (Fig. S11b†) was from the detachment of an H_2O molecule from EMF. Similarly, the m/z of

155.19 (Fig. S11c†) and 171.19 (Fig. S11d†) were assigned to the 2-methyl-5-(ethanolamine methyl) furan (MEMF) and 2-hydroxymethyl-5-(ethanolamine methyl)furan (HEMF), respectively. In addition, the conversion rate of the three amination reactions over time at different potentials was further calculated in Table 1 and Fig. S12†. For FF (Fig. S12a†), 78% conversion efficiency was reached at -0.6 V_{RHE} by equation S6†. Besides, the carbon fiber paper was utilized, which had limited reduction amination efficiency with a poor yield of 15%. In the absence of a catalyst, the reductive amination was quite unsatisfactory. FE (43.7%, equation S8†) was obviously enhanced at a potential of -0.6 V_{RHE} as shown in Fig. S13†, which was much better than the value of 26.1% at -0.4 V_{RHE} and 18.5% at -0.8 V_{RHE}. A similar trend was also observed in the case of HMF. The selectivity of the aldimine reduction was approximately 100% over TiS_2 nanosheets by equation S7† and TON was then used to calculate the effective utilization rate of catalysts by equation S9†, which was defined as mole substrate reacted per mole catalyst. The TON values for the FF reductive amination reaction reached 357 at -0.6 V_{RHE}, while a TON of over 300 for MF and HMF for ERA was reached. To comfire the viability of ERA, ethanediamine as a nitrogen source was used to investigate product. As shown in Fig. S14†, all yields of ONC were over 85%.

In addition, the mass of product per mass of active surface area (MASA) of electrode was also calculated using equation S10†. As shown in Table 1, the MASA in the 5 mM FF electrolyte is 58.6 mg cm^{-2} for EMF at a low potential, 32.9 mg cm^{-2} for MF and 38.9 mg cm^{-2} for HMF, indicating the high-efficiency of ERA within the FF electrolyte and the loss (<0.1 mg) of catalyst during the ERA process was neglectable. When compared to the electrochemical and traditional, *j*, TOF, MASA, and TON were used to construct a comprehensive assessment system for ERA.

Catalyst stability and potential pathway

Catalyst stability was a crucial criterion for a viable process. The typical crystal planes of the catalyst post reaction (Fig. S15†) corresponded well with the specific phase of the fresh TiS_2 nanosheets.[56] During 6 h of ERA, the current curve was stationary at -0.8 V_{RHE} in Fig. S16. Raman spectra (Fig. S17†) also confirmed the high stability of TiS_2 with E_g and A_{1g} modes at 228 cm^{-1} and 330 cm^{-1}, respectively. XPS spectra were subsequently used to compare the structural changes of the pristine and spent TiS_2 electrode. After undergoing the ERA, the two peaks at the binding energies of 161.1 and 162.8 eV in the high-resolution S 2p spectrum correspond to Ti-S and S-S covalent bonds in Fig. S18a and S18b†.[57, 58, 59] In comparison with the fresh electrode, no apparent morphologic change is seen in the SEM images (Fig. S19†). The HR-TEM image (Fig. S18c†) of TiS_2 nanosheets clearly shows a lattice distance of 0.285 nm, corresponding to the (002) crystal face. Fig. S18d† displays the SAED pattern with typical planes of TiS_2. Furthermore, the catalytic performance (Fig. S18e and Fig. S20†) for ERA was executed using the recycled TiS_2 nanosheets. Over five runs of FF aminations, TiS_2 kept over 90% FF conversion with very little mass loss of electrode and over 95% selectivity for EMF. Even after 30 h, only 5% decay was found in the case of MF and HMF.

In order to give an in-depth insight into the ERA reaction, the ERA catalytic process over laminate TiS_2 nanosheets was studied using *in-situ* diffuse reflectance infrared Fourier transform spectroscopy (DRIFTS), as the methodology detailed in SI. The results of DRIFTS measurement as shown in Fig. 5a show that the (C-H) stretching vibrations of the fresh FF were observed at 2810 and 2848 cm^{-1}, compared to the (C-H) stretching vibrations of the amine containing products at 2920 and 2848 cm^{-1}. This result allowed the reaction sequence to be

Table 1 Results obtained from the ERA at various potentials.

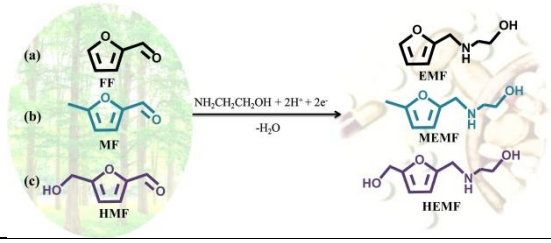

Furanic aldehydes	Potential applied (V_{RHE})	Average current (mA cm^{-2})	Conversion (%)	Selectivity (%)	FE (%)	MASA (mg cm^{-2})	TON
	-0.4	1.45	27	> 99	33.3	58.6	101
FF	-0.6	4.21	90	> 99	38.2	195.5	338
	-0.8	10.52	95	> 99	16.1	206.9	357
	-0.4	0.82	12	> 99	26.1	32.9	42
MF	-0.6	2.94	72	> 99	43.7	197.5	252
	-0.8	8.30	86	> 99	18.5	235.9	301
	-0.4	1.24	14	> 99	20.2	39.9	49
HMF	-0.6	4.57	88	> 99	34.4	251.1	308
	-0.8	8.90	91	> 99	18.3	259.6	318

Note: conversion, selectivity, and FE were calculated using equations S6-S10 (ESI†).

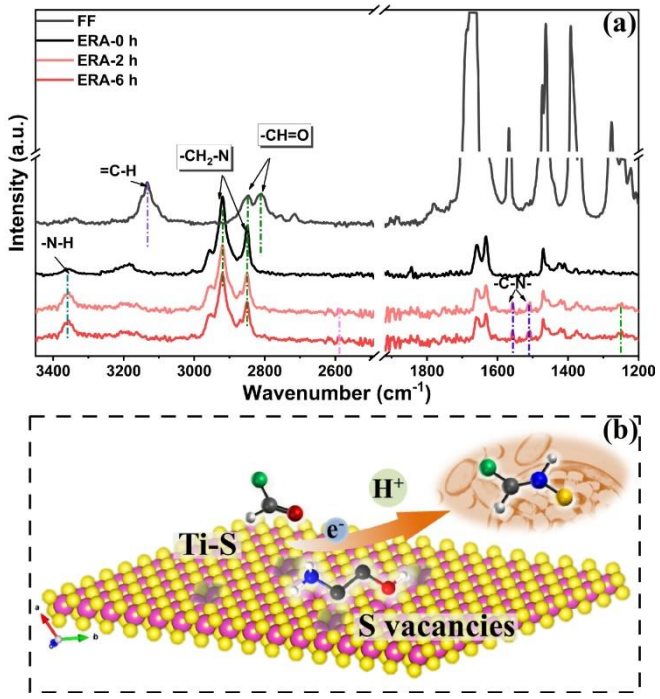

Fig. 5 (a) *In-situ* diffuse reflectance infrared Fourier transform spectroscopy (DRIFTS) of FF and solution during ERA. (b) The proposed reductive amination pathway of furanic aldehydes over TiS_2.

followed via DRIFTS.[60, 61] For the spectra of FF and ethanolamine solution in Fig. S21†, there were two new peaks at 1631 and 1660 cm^{-1}, ascribed to the intermediate in the mixed solution. As reaction time increased, the stretching vibration of the -N-H with C-N species from the product of EMF was found in the 3350 cm^{-1} region, along with the presence of several newly formed bands (1557 cm^{-1} and 1508 cm^{-1}) ascribed to the -C-N stretching vibration of EMF.[24, 62] In addition, a right shift from 1276 and 1250 cm^{-1} of FF to 1257 and 1243 cm^{-1} for ERA described to δ(C-H) of -C=O bond, which is ascribed to FF molecular adsorption on the surface of vacancy-rich TiS_2.[63, 64] After the electrochemical reductive amination reaction, a peak at 2591 cm^{-1} was observed. This peak was attributed to the S-H···O=C interaction between organic molecules and the vacancy-rich TiS_2 nanosheets.[65, 66] Therefore, the ERA reaction with FF reacting over the Sulfur vacancy-rich TiS_2 nanosheets was proposed in Fig. 5b. In the amination reaction, laminate TiS_2 nanosheets have a larger ECSA and a fast reaction kinetics resulting in a left shift of the LSV curve with a high TOF value within 0.7 M ethanolamine and FF electrolyte. Sulfur vacancies on the thin surface can adsorb more reactants and the layered structure of TiS_2 nanosheets would expose more active sites. In the process of the ERA, the aldehyde group was firstly dehydrated with ethanolamine in a nucleophilic reaction to produce the imine. Subsequently, the imine could be quickly reduced to obtain aminofurans through *in-situ* generated H^+ from H_2O accompanied by an electron source. The imine was then hydrogenated by breaking the C=N double bond after gaining an electron. By applying the suitable voltage to generate EMF, MEMF, and HEMF, the direct ERA was further increased.

Conclusions

Laminate 1T-TiS_2 nanosheets with a thickness of 3.86 nm were successfully fabricated and exhibited reliable performance (over 95% conversion with nearly satisfactory selectivity) for the highly selective synthesis of various ONC using biomass-derived furanic aldehydes (e.g. FF, MF, and HMF) at ambient temperature and atmospheric pressure. When 5 mM FF was introduced, the onset potential dramatically shifted toward the positive direction of water reduction. TOF value of 0.407 s^{-1} at -0.5 V_{RHE} was reached, which were much larger than those within ethanolamine electrolytes of 0.205 s^{-1} with MF and 0.287 s^{-1} using HMF. The TiS_2 nanosheets exhibited the highest performance and fastest kinetics of ERA using FF substrate. These were attributed to the largest electrochemical active surface area laminate of 3.25 cm^2 in 5 mM FF, compared with 2.75 cm^2 in 5 mM MF and 3.00 cm^2 in 5 mM HMF.

Through electrochemical C=O activation, we have uncovered the first ERA of C-N that enables the use of sustainable electricity leading to EMF, MEMF and HEMF. Notable features of this work were attributed to the offered more active sites on the thin nanosheets. Importantly, the hydrogen source was from water avoiding the use of chemical reducing agents and ERA achieved the high selectivity of ONC product at ambient temperature/pressure. Over 95% conversion and nearly 100% selectivity with a low overpotential was achieved. Besides, the laminate 1T-TiS2 nanosheets maintained the stable structure and high durability in ERA process. This work provides an eco-friendly and efficient alternative for the synthesis of various ONC from biorefinery.

Experimental section

Controllable synthesis of laminate TiS_2 nanosheets

Purities and chemical sources used in this work are described in the electronic supplementary information (ESI† 1.1). TiS_2 nanosheets were facilely and controllably synthesized by the direct reaction of Ti powder and sulfur powder. The obtained laminated TiS_2 catalysts were further treated by quenching with a solution of ice and water. After that, the exfoliated TiS_2 nanosheets were obtained in isopropanol (20 mL) using ultrasonic. The general procedure is illustrated in Fig. 1 and more details are indicated in the controllable synthesis of TiS_2 nanosheets (ESI †).

Electrochemical synthesis of aminofurans

20 mL of 0.7 M ethanolamine solution (see ESI†) was transferred into a four-necked flask with a volume of 25 mL. The electrochemical testing was conducted using Autolab M204 purchased from Metrohm in a typical three-electrode system with Ar-saturation for the reductive amination. The working electrode (WE) was fabricated by coating TiS_2 nanosheets on carbon fibre paper. Pt wire (Φ = 1 mm, 4 cm of length, Shanghai CH Instruments Ins, China) as counter electrode (CE), and a Hg|HgO (Gaoss Union, Single salt bridge) as reference electrode (RE) was used for all electrochemical reductive amination (ERA) reactions at room temperature and pressure. The acquired potential was standardized to the reversible hydrogen electrode (RHE) according to equation S1

(see ESI†). The scanning linear sweep voltammetry (LSV) curves were investigated at the applied potential range of 0.1 to -1.0 V (vs. RHE) at a scan rate of 5 mV s^{-1}. The ERA reactions were executed in a 0.7 M ethanolamine with and without the different furanic aldehydes of 5 mM FF, MF, and HMF at a constant applied potential with stirring rate of 600 rpm in one compartment. The IR value was compensated for the standing voltage drop between the WE and RE via Nova Software in all the electrochemical tests.

Analysis of products

To analyse quantitatively the concentration of the reactant in ERA, 100 µL of the solution was taken from the homogeneous electrolyte solution during chronoamperometry at -0.4, -0.6 and -0.8 V vs. RHE. The conversion of FF, MF, and HMF were evaluated by high-performance liquid chromatography (HPLC, mode: Shimadzu Prominence LC-20A), with a Shimadzu column (C 18, size: 5 µm, 4.6 × 150 mm) and an ultraviolet-visible detector (265 nm). A mixed mobile phase 5 mM ammonium formate aqueous (70 vol%) and methanol (30 vol%) was used to detect the reaction liquid at a flow rate of 1.0 mL min^{-1}. The injection volume was 10 µL. The species and selectivity of product using multiple-reaction monitoring mode were investigated through ultra-performance liquid chromatography in conjunction with triple-quadrupole tandem mass spectrometry (UPLC-MS/MS). Methods UPLC-MS/MS assay using negative ion mode was implemented by a Waters ACQUITY UPLC CSH™ C18 (2.1 mm × 50 mm Column, 1.7 µm) with the mixed mobile phase including acetonitrile and 0.1% methanoic acid at 0.3 mL min^{-1} by gradient elution. For specific details, acetonitrile dosage was 10% in 0-1 min, 90% in 1.1-3 min, and 10% in 12.1-13 min.

Ex situ X-ray absorption spectroscopy (XAS) measurements

The *X-ray absorption spectroscopy (XAS) measurements* were put into effect at the Ti K-edge (4966 eV) on the B18 beamline at the Diamond Light Source, Didcot, UK. Measurements were carried out in transmission mode utilizing a QEXAFS device with fast-scanning Si (111) double crystal monochromators for the Ti k-edge. The data processing was performed using IFEFFIT with the Demeter package (Athena and Artemis).[67] Fitting parameters: S_0^2=0.707 calculated from the foil, fit range $3 < k(Å^{-2}) < 10.5$, $1.4 < R(Å) < 2.5$; number of independent points = 5.1.

Author Contributions

M.Z.: Electrochemical reaction operation. S.X.: Sample characterization and manuscript revision. M.Z., E.K.G, S.X., M.B. and D.D.: Data curation. Y.H.: Synthesis of material. B.L.: Writing the experiment part. X.L. and Y.W.: Sorting out the supplementary Information. S.X., C.R.A.C., H.L. and K.Y.: Writing - review & editing. C.R.A.C. and K.Y.: Supervision.

Conflicts of interest

There are no conflicts to declare.

Acknowledgements

This work was supported by National Key R&D Program of China (2020YFC1807600), National Natural Science Foundation of China (11922415, 22078374), National Ten Thousand Talent Plan, Guangdong Basic and Applied Basic Research Foundation (2019B1515120058), the Pearl River Scholarship Program of Guangdong Province Universities and Colleges (20191001), and the Scientific and Technological Planning Project of Guangzhou, China (202206010145). We also thank Diamond Light Source for access to the Beamlines B18 and also the Diamond Light Source beamline staff and the UK catalysis Hub Block Allocation Group (BAG) Programme Mode Application, in particular Dr. Veronica Celorrio and Dr. June Callison, for provision of beamtime at B18 (Experiment SP19850-6) for collection of the data and the initial discussion. The UK Catalysis Hub is kindly thanked for resources and support provided via our membership of the UK Catalysis Hub Consortium and funded by EPSRC grant: EP/R026939/1, EP/R026815/1, EP/R026645/1, EP/R027129/1 or EP/M013219/1(biocatalysis).

Notes and references

1 T. Senthamarai, K. Murugesan, J. Schneidewind, N. V. Kalevaru, W. Baumann, H. Neumann, P. C. J. Kamer, M. Beller and R. V. Jagadeesh, *Nature Commun.*, 2018, **9**, 4123.

2 K. Murugesan, V. G. Chandrashekhar, T. Senthamarai, R. V. Jagadeesh and M. Beller, *Nature Protoc.*, 2020, **15**, 1313-1337.

3 R. Kumar, N. J. Flodén, W. G. Whitehurst and M. J. Gaunt, *Nature*, 2020, **581**, 415-420.

4 G. M. Torres, Y. Liu and B. A. Arndtsen, *Science*, 2020, **368**, 318-323.

5 D. T. Smith, M. D. Delost, H. Qureshi, and J. T. Njarðarson, Top 200 Pharmaceuticals by Retail Sales in 2020, https://njardarson.lab.arizona.edu/sites/njardarson.lab.arizona.edu/files/Top%20200%20Pharmaceuticals%20By%20Retail%20Sales%202020V3.pdf, accessed 16/04/2022.

6 S. Song, J. Qu, P. Han, M. J. Hülsey, G. Zhang, Y. Wang, S. Wang, D. Chen, J. Lu and N. Yan, *Nature Commun.*, 2020, **11**, 4899.

7 Q. Hou, X. Qi, M. Zhen, H. Qian, Y. Nie, C. Bai, S. Zhang, X. Bai and M. Ju, *Green Chem.*, 2021, **23**, 119-231.

8 R. V. Jagadeesh, K. Murugesan, A. S. Alshammari, H. Neumann, M.-M. Pohl, J. Radnik and M. Beller, *Science*, 2017, **358**, 326-332.

9 O. I. Afanasyev, E. Kuchuk, D. L. Usanov and D. Chusov, *Chem. Rev.*, 2019, **119**, 11857-11911.

10 X.-P. Fu, P. Han, Y.-Z. Wang, S. Wang and N. Yan, *J. Catal.*, 2021, **399**, 121-131.

11 H. Qi, J. Yang, F. Liu, L. Zhang, J. Yang, X. Liu, L. Li, Y. Su, Y. Liu, R. Hao, A. Wang and T. Zhang, *Nature Commun.*, 2021, **12**, 3295.

12 K. Alorku, C. Shen, Y. Li, Y. Xu, C. Wang and Q. Liu, *Green Chem.*, 2022, **24**, 4201-4236.

13 L. Lin, X. Han, B. Han and S. Yang, *Chem. Soc. Rev.*, 2021, **50**, 11270-11292.

14 N. S. Gould, H. Landfield, B. Dinkelacker, C. Brady, X. Yang and B. Xu, *Chemcatchem*, 2020, **12**, 2106-2115.

15 J. Han and J. Xie, *Chem*, 2020, **6**, 1053-1055.

16 T. Shen and T. H. Lambert, *J. Am. Chem. Soc.*, 2021, **143**, 8597-8602.
17 W. Deng, Y. Wang, S. Zhang, K. M. Gupta, M. J. Hülsey, H. Asakura, L. Liu, Y. Han, E. M. Karp, G. T. Beckham, P. J. Dyson, J. Jiang, T. Tanaka, Y. Wang and N. Yan, *Proc. Natl. Acad. Sci. U.S.A.*, 2018, **115**, 5093-5098.
18 T. Wang, J. Ibañez, K. Wang, L. Fang, M. Sabbe, C. Michel, S. Paul, M. Pera-Titus and P. Sautet, *Nature Catal.*, 2019, **2**, 773-779.
19 C. Lin, J. Zhou, Z. Zheng and J. Chen, *J. Catal.*, 2022, **410**, 164-179.
20 J. G. Pereira, J. M. J. M. Ravasco, J. R. Vale, F. Queda and R. F. A. Gomes, *Green Chem.*, 2022, **24**, 7131-7136.
21 S. Song, V. Fung Kin Yuen, L. Di, Q. Sun, K. Zhou and N. Yan, *Angew. Chem. Int. Edit.*, 2020, **59**, 19846-19850.
22 S. Jiang, E. Muller, F. Jerome, M. Pera-Titus and K. D. O. Vigier, *Green Chem.*, 2020, **22**, 1832-1836.
23 M. Pelckmans, T. Renders, S. Van de Vyver and B. F. Sels, *Green Chem.*, 2017, **19**, 5303-5331.
24 P. V. Rathod, V. G. Deonikar, J. M. C. Puguan and H. Kim, *Fuel*, 2020, **264**, 116822.
25 M. Zhang, Y. Liu, B. Liu, Z. Chen, H. Xu and K. Yan, *ACS Catal.*, 2020, **10**, 5179-5189.
26 M. Yan, Y. Kawamata and P. S. Baran, *Chem. Rev.*, 2017, **117**, 13230-13319.
27 N. Sauermann, R. Mei and L. Ackermann, *Angew. Chem. Int. Edit.*, 2018, **57**, 5090-50947.
28 P. Su, W. Pei, X. Wang, Y. Ma, Q. Jiang, J. Liang, S. Zhou, J. Zhao, J. Liu and G. Q. Lu, *Angew. Chem. Int. Edit.*, 2021, **60**, 16044-16050.
29 H. Zou and J. Chen, *Appl. Catal., B*, 2022, **309**, 121262.
30 L. Du, L. Xing, G. Zhang, X. Liu, D. Rawach and S. Sun, *SusMat*, 2021, **1**, 150-173.
31 T. Gross, A. M. Seayad, M. Ahmad and M. Beller, *Org. Lett.*, 2002, **4**, 2055-2058.
32 Q. Yang, Y. Li, C. Ma, P. Fang, X. Zhang and T. Mei, *J. Am. Chem. Soc.*, 2017, **139**, 3293-3298.
33 J. J. Roylance and K.-S. Choi, *Green Chem.*, 2016, **18**, 5412-5417.
34 Z. Zheng, L. Yu, M. Gao, X. Chen, W. Zhou, C. Ma, L. Wu, J. Zhu, X. Meng, J. Hu, Y. Tu, S. Wu, J. Mao, Z. Tian and D. Deng, *Nature Commun.*, 2020, **11**, 3315.
35 M. Wu, G. Zhang, H. Tong, X. Liu, L. Du, N. Chen, J. Wang, T. Sun, T. Regier and S. Sun, *Nano Energy*, 2021, **79**, 105409.
36 Q. Fu, J. Han, X. Wang, P. Xu, T. Yao, J. Zhong, W. Zhong, S. Liu, T. Gao, Z. Zhang, L. Xu and B. Song, *Adv. Mater.*, 2021, **33**, 1907818.
37 M. Zhang, Y. He, D. Yan, H. Xu, A. Wang, Z. Chen, S. Wang, H. Luo and K. Yan, *Nanoscale.*, 2019, **11**, 22255-22260.
38 J. Zhang, J. Wu, H. Guo, W. Chen, J. Yuan, U. Martinez, G. Gupta, A. Mohite, P. M. Ajayan and J. Lou, *Adv. Mater.*, 2017, **29**, 1701955.
39 J. Lu, F. Lian, Y. Zhang, N. Chen, Y. Li, F. Ding and X. Liu, *J. Mater. Chem. A*, 2020, **8**, 6532-6538.
40 Y. Wang, Z. Zhang, Y. Mao and X. Wang, *Energy Environ. Sci.*, 2020, **13**, 3993-4016.
41 Y. Takahashi, Y. Kobayashi, Z. Wang, Y. Ito, M. Ota, H. Ida, A. Kumatani, K. Miyazawa, T. Fujita, H. Shiku, Y. E. Korchev, Y. Miyata, T. Fukuma, M. Chen and T. Matsue, *Angew. Chem. Int. Edit.*, 2020, **59**, 3601-36087; Angew. Chem. 2020, **132**, 33629-33636.
42 T. Lei, M. Xianguang, D. Dehui and B. Xinhe, *Adv. Mater.*, 2019, **31**, 1901996.
43 Z. Chen, G. Zhang, H. Chen, J. Prakash, Y. Zheng and S. Sun, *Renewable and Sustainable Energy Reviews*, 2022, **155**, 111922.
44 Y. Liu, J. Wu, K. P. Hackenberg, J. Zhang, Y. M. Wang, Y. Yang, K. Keyshar, J. Gu, T. Ogitsu, R. Vajtai, J. Lou, P. M. Ajayan, B. C. Wood and B. I. Yakobson, *Nature Energy*, 2017, **2**, 17127.
45 G. M. Carroll, H. Zhang, J. R. Dunklin, E. M. Miller, N. R. Neale and J. van de Lagemaat, *Energy Environ. Sci.*, 2019, **12**, 1648-1656.
46 X. Meng, C. Ma, L. Jiang, R. Si, X. Meng, Y. Tu, L. Yu, X. Bao and D. Deng, *Angew. Chem. Int. Edit.*, 2020, **59**, 10502-10507.
47 K. L. Zhou, C. B. Han, Z. Wang, X. Ke, C. Wang, Y. Jin, Q. Zhang, J. Liu, H. Wang and H. Yan, *Adv. Sci.*, 2021, **8**, 2100347.
48 L. Wang, J. Zou, S. Chen, G. Zhou, J. Bai, P. Gao, Y. Wang, X. Yu, J. Li, Y.-S. Hu and H. Li, *Energy Storage Mater.*, 2018, **12**, 216-222.
49 X. Lu, K. Xu, S. Tao, Z. Shao, X. Peng, W. Bi, P. Chen, H. Ding, W. Chu, C. Wu and Y. Xie, *Chem. Sci.*, 2016, **7**, 1462-1467.
50 H. Tao, M. Zhou, R. Wang, K. Wang, S. Cheng and K. Jiang, *Adv. Sci.*, 2018, **5**, 1801021.
51 X. Huang, J. Tang, B. Luo, R. Knibbe, T. Lin, H. Hu, M. Rana, Y. Hu, X. Zhu, Q. Gu, D. Wang and L. Wang, *Adv. Energy Mater.*, 2019, **9**, 1901872.
52 P. C. Sherrell, K. Sharda, C. Grotta, J. Ranalli, M. S. Sokolikova, F. M. Pesci, P. Palczynski, V. L. Bemmer and C. Mattevi, *ACS Omega*, 2018, **3**, 8655-8662.
53 G. A. Tritsaris, E. Kaxiras, S. Meng and E. Wang, *Nano Lett.*, 2013, **13**, 2258-2263.
54 M. Inoue, H. P. Hughes and A. D. Yoffe, *Adv. Phys.*, 1989, **38**, 565-604.
55 A. Maiti and S. K. Srivastava, *J. Mater. Chem. A*, 2018, **6**, 19712-19726.
56 T. Liu, N. Peng, X. Zhang, R. Zheng, M. Xia, H. Yu, M. Shui, Y. Xie and J. Shu, *Nano Energy*, 2021, **79**, 105460.
57 J. Tang, X. Huang, T. Lin, T. Qiu, H. Huang, X. Zhu, Q. Gu, B. Luo and L. Wang, *Energy Storage Mater.*, 2020, **26**, 550-559.
58 C. W. Lin, X. J. Zhu, J. Feng, C. Z. Wu, S. L. Hu, J. Peng, Y. Q. Guo, L. L. Peng, J. Y. Zhao, J. L. Huang, J. L. Yang and Y. Xie, *J. Am. Chem. Soc.*, 2013, **135**, 5144-5151.
59 Z. Hu, Z. Tai, Q. Liu, S.-W. Wang, H. Jin, S. Wang, W. Lai, M. Chen, L. Li, L. Chen, Z. Tao and S.-L. Chou, *Adv. Energy Mater.*, 2019, **9**, 201803210.
60 O. Kikhtyanin, V. Korolova, A. Spencer, L. Dubnová, B. Shumeiko and D. Kubička, *Catal. Today*, 2021, **367**, 248-257.
61 Y. Wang, S. Furukawa, Z. Zhang, L. Torrente-Murciano, S. A. Khan and N. Yan, *Cataly. Sci. Technol.*, 2019, **9**, 86-96.
62 K. Kaiden, T. Matsui and S. Tanaka, *Appl. Spectrosc.*, 1987, **41**, 180-184.
63 L. Luo, Z. Wang, X. Xiang, D. Yan and J. Ye, *ACS Catal.*, 2020, **10**, 4906-4913.
64 H. Liu, W. Jia, X. Yu, X. Tang, X. Zeng, Y. Sun, T. Lei, H. Fang, T. Li and L. Lin, *ACS Catal.*, 2021, **11**, 7828-7844.
65 M. S. Rozenberg, T. Nishio and T. Steiner, *New J. Chem.*, 1999, **23**, 585-586.
66 A. Mielcarek and A. Dołęga, *J. Mol. Struct.*, 2016, **1103**, 217-223.
67 B. Ravel and M. Newville, *J. Synchrotron Rad.*, 2005, **12**, 537-541.